Article

Free-Energy-Based Discrete Unified Gas Kinetic Scheme for van der Waals Fluid

Zeren Yang [1], Sha Liu [1,2], Congshan Zhuo [1,2] and Chengwen Zhong [1,2,*]

1   School of Aeronautics, Northwestern Polytechnical University, Xi'an 710072, China
2   National Key Laboratory of Science and Technology on Aerodynamic Design and Research,
    Northwestern Polytechnical University, Xi'an 710072, China
*   Correspondence: zhongcw@nwpu.edu.cn

Abstract: The multiphase model based on free-energy theory has been experiencing long-term prosperity for its solid foundation and succinct implementation. To identify the main hindrance to developing a free-energy-based discrete unified gas-kinetic scheme (DUGKS), we introduced the classical lattice Boltzmann free-energy model into the DUGKS implemented with different flux reconstruction schemes. It is found that the force imbalance amplified by the reconstruction errors prevents the direct application of the free-energy model to the DUGKS. By coupling the well-balanced free-energy model with the DUGKS, the influences of the amplified force imbalance are entirely removed. Comparative results demonstrated a consistent performance of the well-balanced DUGKS despite the reconstruction schemes utilized. The capability of the DUGKS coupled with the well-balanced free-energy model was quantitatively validated by the coexisting density curves and Laplace's law. In the quiescent droplet test, the magnitude of spurious currents is reduced to a machine accuracy of 10^{-15}. Aside from the excellent performance of the well-balanced DUGKS in predicting steady-state multiphase flows, the spinodal decomposition test and the droplet coalescence test revealed its stability problems in dealing with transient flows. Further improvements are required on this point.

Keywords: free-energy model; discrete unified gas-kinetic scheme; multiphase flow; flux reconstruction

1. Introduction

Multiphase fluid flow characterized by the concurrent presence of multiple thermodynamic phases is frequently encountered in industrial processes and engineering applications. Insightful understanding of the multiphase flow behavior could facilitate improvements in manufacturing technology and production efficiency. Due to the restriction on measurement technology and the experimental platform, it is particularly challenging to reveal the flow details by experimental methods. Benefiting from the substantial improvements in computing power, numerical simulation technology has been developed into a powerful tool for the study of complicated behaviors arising in multiphase fluid flow. By numerically solving the set of interface capturing and hydrodynamic equations, a multitude of research studies [1–4] vividly detail the interface dynamics and flow structures from a macroscopic perspective. Essentially, the interfacial phenomenon represents the macroscopic manifestation of the microscopic interactions among fluid molecules [5]. Numerical methods based on realistic microscopic physics could offer in-depth findings regarding multiphase phenomena, but the heavy computational requirement of such methods for industry-scale multiphase problems is far beyond affordable. In recent years, numerical schemes constructed with the mesoscopic theory [6] have been emerging as a compelling methodology for resolving multiphase flow patterns as this bridges the gap between the macroscopic descriptions of multiphase dynamics and microscopic intermolecular interactions and, thus, generates insightful understandings at an affordable cost.

Among various previously proposed mesoscopic approaches [7–9], the lattice Boltzmann (LB) method [7] has received particular attention for its concise and intuitive way of representing intermolecular interactions. Generally, the lattice Boltzmann multiphase models developed in the past few decades can be categorized into four classifications: the color-gradient model [10], the phase-field model [11,12], the pseudopotential model [13], and the free-energy model [14]. The phase-field model employs independent sets of distribution functions to separately transfer mass and momentum, which could cause mass non-conservation problems near the interface region [15]. The pseudopotential model and the free-energy model employ a single set of distribution functions to ensure a coherent transport of mass and momentum, which conforms to the physical reality that mass and momentum are simultaneously transferred by the unique molecules. Compared to the pseudopotential model, where interactions are built heuristically, the free-energy model is constructed upon the stationary-action principle, which possesses a firm physical background. Over the last couple of decades, the free-energy lattice Boltzmann method has been successfully applied to numerically tackle a variety of flow issues including the contact line movement [16,17], multicomponent fluids' flow [18,19], wetting boundaries [20,21], and large-density-ratio fluid flow [22,23]. The primitive free-energy multiphase model proposed by Swift et al. [14] reflects the interaction effects via a modified equilibrium distribution function, whose second-order moment incorporates a nonideal thermodynamic pressure tensor. However, this primitive model suffers from a lack of Galilean invariance due to the superfluous terms recovered in the momentum equation. Later, Swift et al. [24] tried to remedy this defect by introducing additional terms to the pressure tensor, but an analysis through the Chapman–Enskog expansion demonstrated that the lack of Galilean invariance cannot be entirely eliminated. Based on Swift et al.'s work, Inamuro et al. [25] proposed a Galilean-invariant free-energy model with the guidance of asymptotic theory. Kalarakis et al. [26] restored the Galilean invariance of the free-energy model to second-order accuracy by modifying the zero-order momentum flux tensor. Wagner and Li [27] replaced the contribution of the nonideal pressure tensor with a corrected force term and improved the Galilean invariance of the model in large velocity situations. Meanwhile, Lee and Fischer [28] reformulated the pressure form of the interaction force into a potential form and reduced the magnitude of the spurious velocity to a machine level, at the cost of including the information in next-nearest-neighbor cells. Subsequently, Guo et al. [5] spotted that the spurious velocity originates from the force imbalance at the discrete level. Based on this finding, Lou and Guo [29] applied the Lax–Wendroff scheme to the lattice Boltzmann free-energy model and successfully mitigated the effects of the force imbalance. Very recently, Guo [30] proposed a well-balanced lattice Boltzmann scheme with which the spurious velocity can be ultimately minimized to the machine accuracy. The previously mentioned improvements were carried out within the framework of the lattice Boltzmann method, which inherits its advantages such as great simplicity and high efficiency. However, the uniformity requirement on the grid types posed by the LB method prevents its application in industrial cases.

Developed in the framework of the finite volume method, the discrete unified gas-kinetic scheme (DUGKS) [31] suffers no restriction in terms of the grid types. With the information of the Knudsen number incorporated in the construction of the interface flux, the DUGKS exhibits the capability of properly modeling a wide range of fluid flows ranging from the continuum regime to the free-molecule regime [32]. Over the past decade, the DUGKS has proven its excellent performance in predicting microscale gas flows [33,34], multicomponent gas flows [35,36], turbulent flows [37–39], compressible flows [40–42], radiative heat transfer [43,44], and so forth [45]. A comparative study [46] has demonstrated the stability superiority of the DUGKS over that of the LB method in terms of nearly incompressible flows. However, the DUGKS studies centered on multiphase fluid flows remain limited [47,48] and the multiphase DUGKS has been primarily confined to the phase-field model [49]. Although Yang et al. [50] developed a pseudopotential-based DUGKS for binary fluid flow, a free parameter is needed to guarantee the isotropic prop-

erty of the fluid interface. Inspired by the well-balanced LB scheme [30], Zeng et al. [51] proposed a well-balanced DUGKS for two-phase fluid flows using the free-energy model. Comparative results demonstrated the superior performance of the DUGKS over that of the LB method. Nevertheless, there is still a lack of an insightful comprehension as to the isotropic property of free-energy-based DUGKS. In this research, we elucidate the mechanism for the nonisotropic phenomena produced by the free-energy-based DUGKS using different reconstruction approaches. Then, we couple the well-balanced free-energy model with the DUGKS implemented with different reconstruction schemes to investigate practical van der Waals (vdW) fluid flows. The rest of this paper is organized as follows. In Section 2, the primitive and the well-balanced free-energy models are introduced, followed by the detailed explanation of the Strang-splitting DUGKS. The comparative numerical results, as well as brief discussions are presented in Section 3. Finally, a summary is given in Section 4.

2. Numerical Methodology

In this section, the first part theoretically introduces the free-energy model based on the vdW chemical potential and the second part exhaustively explains the Strang-splitting DUGKS implemented with different reconstruction schemes.

2.1. Free-Energy Model

Considering a multiphase system, the free-energy functional in terms of the fluid density ρ can be expressed as [14,24]

$$\mathcal{F} = \int \phi(\rho, \nabla \rho) d\Omega_V = \int \left(E_f(\rho) + \frac{\kappa}{2} |\nabla \rho|^2 \right) d\Omega_V, \tag{1}$$

where Ω_V is the spatial region occupied by the system, $\phi(\rho, \nabla \rho)$ denotes the total free-energy density, in which $E_f(\rho)$ represents the bulk free-energy density, and $\frac{\kappa}{2} |\nabla \rho|^2$ signifies the interface free-energy density. The parameter κ is a positive constant determined by the interface thickness and the surface tension coefficient. Minimization of the free-energy $\mathcal{F}$ that is subject to the constraint of a constant mass $\mathcal{M}$ evolves the system towards the equilibrium condition, where

$$\mathcal{M} = \int \rho d\Omega_v. \tag{2}$$

To impose the mass constraint, a transformed free-energy functional $\mathcal{L}$ is constructed using the method of Lagrange multipliers:

$$\mathcal{L} = \mathcal{F} - \lambda \mathcal{M}, \tag{3}$$

where λ is the Lagrange multiplier. Minimization of the constrained free-energy demands the corresponding first variation to be zero:

$$\delta \mathcal{L} = 0, \tag{4}$$

which yields the following Euler–Lagrange equation:

$$\frac{\partial \psi}{\partial \rho} - \nabla \cdot \left(\frac{\partial \psi}{\partial (\nabla \rho)} \right) = \frac{dE_f}{d\rho} - \kappa \nabla^2 \rho - \lambda = 0, \tag{5}$$

where

$$\psi(\rho, \nabla \rho) = \phi(\rho, \nabla \rho) - \lambda \rho. \tag{6}$$

The chemical potential μ_c is defined as the variation of the free-energy $\mathcal{F}$ with respect to the density [52]:

$$\mu_c = \frac{\delta \mathcal{F}}{\delta \rho} = \frac{dE_f}{d\rho} - \kappa \nabla^2 \rho. \tag{7}$$

As the integrand of transformed free-energy $\mathcal{L}$ does not explicitly contain any spatial coordinates, it remains invariant regardless of the spatial translations [3]. Noether's theorem [53] says that the invariance of the free-energy with respect to spatial translations corresponds to a conserved tensorial current J satisfying [54]:

$$\nabla \cdot J = 0, \tag{8}$$

where J is a second-rank tensor given by

$$J = -\psi I + \nabla\rho \otimes \frac{\partial \psi(\rho, \nabla\rho)}{\partial(\nabla\rho)}, \tag{9}$$

in which I is the identity matrix. Substituting Equations (5) and (6) into Equation (9) leads to

$$J = \left(\rho\mu_c - E_f - \frac{\kappa}{2}|\nabla\rho|^2\right)I + \kappa\nabla\rho\nabla\rho. \tag{10}$$

The bulk pressure p_b is connected to the bulk free-energy density E_f via the Legendre transform [54]:

$$p_b(\rho) = \rho\frac{dE_f}{d\rho} - E_f(\rho), \tag{11}$$

with which the conserved current tenor J can be identified as the thermodynamic pressure tensor P in such a way that

$$P \equiv J = \left(p_b - \kappa\rho\nabla^2\rho - \frac{\kappa}{2}|\nabla\rho|^2\right)I + \kappa\nabla\rho\nabla\rho. \tag{12}$$

With some basic algebraic manipulations, the divergence of the pressure tensor can be simplified as

$$\nabla \cdot P = \rho\nabla\mu_c. \tag{13}$$

In the traditional free-energy model [28], the total effects of excess pressure accounting for the phase interactions can be represented by the following interaction force

$$F = \nabla \cdot P_0 - \nabla \cdot P = \nabla p_0 - \rho\nabla\mu_c, \tag{14}$$

where $P_0 = p_0 I$ denotes the pressure tensor of an ideal gas. In the well-balanced free-energy model [30], the interaction force is defined as

$$F = -\rho\nabla\mu_c \tag{15}$$

in order to eliminate the force imbalance at the discrete level.

The only remaining task is to determine the bulk free-energy density E_f. In the work of Zeng et al. [51], E_f takes a double-well form, which relates to no specific equation of state (EOS). In the current research, the bulk pressure is evaluated by the nonideal van der Waals EOS [55] expressed as

$$p_b = \frac{\rho RT}{1 - b\rho} - a\rho^2, \tag{16}$$

where parameter a denotes the intermolecular interaction strength, parameter b indicates the volume correction, R stands for the gas constant, and T represents the temperature. The corresponding bulk free-energy density can be obtained by solving Equation (11):

$$E_f(\rho) = \rho RT\ln\left(\frac{\rho}{1 - b\rho}\right) - a\rho^2. \tag{17}$$

The chemical potential can then be obtained according to Equation (7):

$$\mu_c = RT\left[\ln\left(\frac{\rho}{1-b\rho} + \frac{1}{1-b\rho}\right)\right] - 2a\rho - \kappa\nabla^2\rho, \tag{18}$$

with which the interaction force $\boldsymbol{F}$ can be evaluated. In the current research, the parameters in the vdW-EOS were set as [56] $a = 9/392, b = 2/21, R = 1$. κ was fixed at 0.02 if not otherwise specified. The critical density and temperature are given as $\rho_c = 3.5$ and $T_c = 1/14$.

2.2. Strang-Splitting DUGKS

In this subsection, the evolution process of the discrete unified gas-kinetic scheme is exhaustively clarified. Then, the Strang-splitting scheme for the incorporation of the interaction force is introduced.

2.2.1. Discrete Unified Gas-Kinetic Scheme

The investigation of multiphase flow problems in the current research was conducted by numerically solving the Boltzmann-BGK equation:

$$\frac{\partial f}{\partial t} + \boldsymbol{\xi} \cdot \nabla_x f = \Omega \equiv -\frac{f - f^E}{\tau}, \tag{19}$$

where $f = f(\boldsymbol{x}, \boldsymbol{\xi}, t)$ denotes the distribution function (DF), referring to a cluster of particles residing at position $\boldsymbol{x}$ with a velocity of $\boldsymbol{\xi}$ at time t, τ indicates the relaxation time, and f^E represents the Maxwellian distribution function approached by f within each collision. The nondimensionalization of Equation (19) is presented in the Appendix A. The moments of distribution functions correspond to the conservative flow variables via

$$\rho = \int f d\boldsymbol{\xi} = \int f^E d\boldsymbol{\xi}, \ \rho\boldsymbol{u} = \int \boldsymbol{\xi} f d\boldsymbol{\xi} = \int \boldsymbol{\xi} f^E d\boldsymbol{\xi}, \tag{20}$$

where $\boldsymbol{u}$ denotes the velocity of the flow field. To numerically solve Equation (19), discretization of the physical and velocity space is a prerequisite. To determine the discrete velocity points along each single dimension, the three-point Gauss–Hermite quadrature is employed. The two-dimensional discrete velocity points can be derived from the tensor product of the single-dimensional velocities, which turns out to be the D2V9 velocity model commonly used in the LB community:

$$\boldsymbol{\xi}_i = \sqrt{3c_s^2}\begin{bmatrix} 0 & 1 & 0 & -1 & 0 & 1 & -1 & -1 & 1 \\ 0 & 0 & 1 & 0 & -1 & 1 & 1 & -1 & -1 \end{bmatrix},$$

where $\boldsymbol{\xi}_i$ is the ith discrete velocity and $c_s = 1/\sqrt{3}$ is the model speed of sound. The ideal gas pressure p_0 shown in Equation (14) relates to the density ρ through $p_0 = \rho c_s^2$.

With the discretization of the velocity space, the Boltzmann-BGK equation turns into

$$\frac{\partial f_i}{\partial t} + \boldsymbol{\xi}_i \cdot \nabla_x f_i = \Omega_i \equiv -\frac{f_i - f_i^E}{\tau}, \tag{21}$$

where the subscript i indicates the distribution function for particles possessing a velocity of $\boldsymbol{\xi}_i$. Subdividing the physical space into a set of grid cells and integrating Equation (21) over a certain cell lead to

$$\frac{d}{dt}\int_{V_c} f_i(\boldsymbol{x}, t)d\boldsymbol{x} + \int_{\partial V_c}(\boldsymbol{\xi} \cdot \boldsymbol{n})f_i(\boldsymbol{x}, t)dS = \int_{V_c} \Omega_i(\boldsymbol{x}, t)d\boldsymbol{x}, \tag{22}$$

where V_c denotes the integral cell centered at position x_c, ∂V_c denotes the surface boundary of the cell, dS is the surface element, and $\boldsymbol{n}$ is the unit vector normal to the surface element. Integrating Equation (22) over a time step of length $\Delta t = t_{n+1} - t_n$ yields

$$f_i^{n+1} - f_i^n + \frac{\Delta t}{|V_c|} F_i^{n+1/2} = \frac{\Delta t}{2} \left[\Omega_i^{n+1} + \Omega_i^n \right], \tag{23}$$

where $|V_c|$ measures the volume of cell V_c and f_i^n and Ω_i^n approximate the cell averages of V_c in such a way that

$$f_i^n = \frac{1}{|V_c|} \int_{V_c} f_i(x, t_n) dx, \tag{24a}$$

$$\Omega_i^n = \frac{1}{|V_c|} \int_{V_c} \Omega_i(x, t_n) dx. \tag{24b}$$

$F_i^{n+1/2}$ measures the kinetic flux at the mid-time $t_n + \Delta t/2$ by

$$F_i^{n+1/2} = \int_{\partial V_c} (\boldsymbol{\xi}_i \cdot \boldsymbol{n}) f_i(x, t_n + \Delta t/2) dS. \tag{25}$$

Note that the midpoint rule is applied to compute the time integral of the kinetic flux and the trapezoidal rule is applied to evaluate the time integral of the collision term in Equation (23). To remove the implicit treatment of the collision term, two auxiliary distribution functions are introduced:

$$\tilde{f}_i = f_i - \frac{\Delta t}{2} \Omega_i, \tilde{f}_i^+ = f_i + \frac{\Delta t}{2} \Omega_i. \tag{26}$$

Substituting Equation (26) into Equation (23), we obtain a fully explicit evolution equation:

$$\tilde{f}_i^{n+1} = \tilde{f}_i^{+,n} + \frac{\Delta t}{2} F_i^{n+1/2}. \tag{27}$$

To obtain the kinetic flux $F_i^{n+1/2}$, the primitive distribution function $f_i(x_f, t_{n+1/2})$ on the cell surface needs to be first evaluated. To this end, we integrate Equation (21) along the characteristic line over a time step length of $\delta t = \Delta t/2$:

$$f_i(x_f, t_{n+1/2}) - f_i(x_f - \boldsymbol{\xi}_i \delta t, t_n) = \frac{\delta t}{2} \left[\Omega_i(x_f, t_{n+1/2}) + \Omega_i(x_f - \boldsymbol{\xi}_i \delta t, t_n) \right]. \tag{28}$$

Note that the trapezoidal rule is once again applied for the time integral of the collision term. Similar to the treatment of Equation (23), the implicitness of Equation (28) is eliminated with the help of the following auxiliary distribution functions:

$$\bar{f} = f - \frac{\delta t}{2} \Omega, \bar{f}^+ = f + \frac{\delta t}{2} \Omega. \tag{29}$$

Equation (28) can then be rearranged as

$$\bar{f}_i(x_f, t_{n+1/2}) = \bar{f}_i^+(x_f - \boldsymbol{\xi}_i \delta t, t_n). \tag{30}$$

The auxiliary distribution function $\bar{f}_i^+(x_f - \boldsymbol{\xi}_i \delta t, t_n)$ on the right-hand side of Equation (30) can be interpolated from the cell-centered $\bar{f}_i^+(x_c, t_n)$, which could be directly constructed via Equation (29). Based on the expansion point of the Taylor series [57], the reconstruction schemes can be classified into the face-based reconstruction scheme (FRS) or the cell-based reconstruction scheme (CRS). The FRS takes the form of

$$\bar{f}_i^+(x_f - \boldsymbol{\xi}_i \delta t, t_n) = \bar{f}_i^+(x_f, t_n) - \boldsymbol{\xi}_i \delta t \cdot \nabla \bar{f}_i^+(x_f, t_n), \tag{31}$$

in which the face-centered $f_i^+(x_f, t_n)$ can be reconstructed from the cell-centered $f_i^+(x_c, t_n)$ via the central difference (CD) scheme [31] or the weighted essentially non-oscillatory (WENO) scheme [58]. The upwind CRS takes the form of

$$\bar{f}_i^+(x_f - \xi_i \delta t) = \begin{cases} \bar{f}_i^+(x_l) + (\delta x_l - \xi_i \delta t) \cdot \nabla \bar{f}_i^+(x_l) + (\delta x_l - \xi_i \delta t)^2 : \nabla^2 \bar{f}_i^+(x_l)/2, & \xi_i \cdot n \le 0, \\ \bar{f}_i^+(x_r) + (\delta x_r - \xi_i \delta t) \cdot \nabla \bar{f}_i^+(x_r) + (\delta x_r - \xi_i \delta t)^2 : \nabla^2 \bar{f}_i^+(x_r)/2, & \xi_i \cdot n > 0, \end{cases} \quad (32)$$

where $\delta x_l = x_f - x_l$ measures the distance from the face center x_f to the adjacent cell center x_l on one side, while $\delta x_r = x_f - x_r$ measures the distance from the face center x_f to the adjacent cell center x_r on the other side. An average value is used if $\xi_i \cdot n = 0$. After finishing the reconstruction of $\bar{f}_i^+(x_f - \xi_i \delta t, t_n)$, the face-centered auxiliary distribution function $\bar{f}_i(x_f, t_{n+1/2})$ can be directly obtained via Equation (30). With a straightforward transformation of Equation (29), the primitive distribution function $f_i(x_f, t_{n+1/2})$ can be calculated by

$$f = \frac{2\tau}{2\tau + \delta t}\bar{f} + \frac{\delta t}{2\tau + \delta t}f^{\mathrm{E}}. \quad (33)$$

The kinetic flux $F_i^{n+1/2}$ can then be evaluated by its definition. After that, the auxiliary distribution function $\tilde{f}_i(x_c, t_{n+1})$ at the next time step can be updated by Equation (27). Similarly, with a transformation of Equation (26), the primitive distribution function can be calculated by

$$f = \frac{2\tau}{2\tau + \Delta t}\tilde{f} + \frac{\Delta t}{2\tau + \Delta t}f^{\mathrm{E}}. \quad (34)$$

The equilibrium distribution function f_i^{E} for the primitive free-energy model is expressed as

$$f_i^{\mathrm{E}} = \omega_i \rho \left[1 + \frac{\xi_i \cdot u}{c_s^2} + \frac{uu : (\xi_i \xi_i - c_s^2 I)}{2c_s^4} \right], \quad (35)$$

where $\omega_i = 4/9$ for $i = 0$, $\omega_i = 1/9$ for $i = \{1, 2, 3, 4\}$, and $\omega_i = 1/36$ for $i = \{5, 6, 7, 8\}$. The equilibrium distribution function f_i^{E} for the well-balanced free-energy model is defined as

$$f_i^{\mathrm{E}} = \begin{cases} \rho + \omega_0 \rho s_0(u), & i = 0, \\ \omega_i \rho s_i(u), & i \ne 0, \end{cases} \quad (36)$$

where

$$s_i(u) = \left[\frac{\xi_i \cdot u}{c_s^2} + \frac{uu : (\xi_i \xi_i - c_s^2 I)}{2c_s^4} \right]. \quad (37)$$

Obviously, the information of macroscopic conservative variables should be first evaluated for the updating of the equilibrium distribution function. Considering the relationship between the auxiliary DF and the primitive DF presented in Equations (26) and (29), the cell-centered conservative variables are updated by

$$\rho = \sum_i f_i = \sum_i \tilde{f}_i, \quad \rho u = \sum_i \xi_i f_i = \sum_i \xi_i \tilde{f}_i, \quad (38)$$

and the face-centered conservative variables are updated by

$$\rho = \sum_i f_i = \sum_i \bar{f}_i, \quad \rho u = \sum_i \xi_i f_i = \sum_i \xi_i \bar{f}_i. \quad (39)$$

The time step length Δt is determined by the Courant–Friedrichs–Lewy (CFL) condition:

$$\Delta t = C \frac{\Delta x}{\sqrt{3c_s^2}}, \quad (40)$$

where C denotes the CFL number and Δx measures the grid spacing.

2.2.2. Strang-Splitting Scheme

To date, the evolution process of DUGKS without considering force terms has been exhaustively clarified. To incorporate the interaction effects between different phases, a source distribution function f_i^S accounting for the force effects is introduced. To correctly recover the macroscopic hydrodynamic equation, the expression of f_i^S for the primitive free-energy model is defined as

$$f_i^S = \omega_i \left[\frac{\boldsymbol{\xi}_i \cdot \boldsymbol{F}}{c_s^2} + \frac{\boldsymbol{u}\boldsymbol{F} : (\boldsymbol{\xi}_i\boldsymbol{\xi}_i - c_s^2\boldsymbol{I})}{c_s^4} \right],$$ (41)

where $\boldsymbol{F}$ is the interaction force defined in Equation (14). The expression of f_i^S for the well-balanced free-energy model is defined as

$$f_i^S = \omega_i \left[\frac{\boldsymbol{\xi}_i \cdot \boldsymbol{F}}{c_s^2} + \frac{\boldsymbol{u}(\boldsymbol{F} + c_s^2\boldsymbol{\nabla}\rho) : (\boldsymbol{\xi}_i\boldsymbol{\xi}_i - c_s^2\boldsymbol{I})}{c_s^4} + \frac{1}{2}\left(\frac{\boldsymbol{\xi}_i^2}{c_s^2} - D\right)(\boldsymbol{u} \cdot \boldsymbol{\nabla}\rho) \right],$$ (42)

where $D = 2$ is the spatial dimension. To circumvent the calculation of the interaction force on the cell interface, the Strang-splitting scheme is employed [59]. With such a treatment, the force effects are considered before and after the evolution process of the DUGKS:

$$\frac{\partial f_i}{\partial t} = \frac{1}{2}f_i^S,$$ (43a)

$$\frac{\partial f_i}{\partial t} + \boldsymbol{\xi}_i \cdot \boldsymbol{\nabla}_x f_i = \Omega_i \equiv -\frac{f_i - f_i^E}{\tau},$$ (43b)

$$\frac{\partial f_i}{\partial t} = \frac{1}{2}f_i^S,$$ (43c)

As Equation (43b) remains identical to Equation (21), it can be solved by the DUGKS procedure addressed previously. Equations (43a) and (43c) can be numerically solved by the forward Euler method:

$$f_i^* = f_i^n + \frac{\Delta t}{2} f_i^{S,n}.$$ (44)

The conservative variables should be accordingly updated via

$$\rho^* = \rho^n, \boldsymbol{u}^* = \boldsymbol{u}^n + \frac{\Delta t}{2}\frac{\boldsymbol{F}^n}{\rho^n}.$$ (45)

The gradient operator and Laplacian operator appearing in Equations (7), (14) and (15) are implemented via the isotropic difference scheme [60].

3. Numerical Results

In this section, several numerical tests are conducted by the Strang-splitting DUGKS to compare the performance of the primitive free-energy model and that of the well-balanced free-energy model. The nonisotropic property caused by the reconstruction procedure in the DUGKS is especially discussed. For steady tests, the iteration terminates once the L_2-norm error satisfies

$$E(\boldsymbol{Q}) = \sqrt{\frac{\sum_x |\boldsymbol{Q}(\boldsymbol{x}, t_n) - \boldsymbol{Q}(\boldsymbol{x}, t_{n-1000})|^2}{\sum_x |\boldsymbol{Q}(\boldsymbol{x}, t_n)|^2}} < e,$$ (46)

where $\boldsymbol{Q}$ is either the flow density ρ or the flow velocity $\boldsymbol{u}$, t_{n-1000} denotes the moment 1,000 time steps ahead of t_n, and e is the error threshold.

3.1. Flat Interface

As a benchmark test, the flat interface has been widely applied to validate the performance of newly proposed models [30,55,56]. The computational domain is a $L_0 \times 16L_0$ rectangular region with $L_0 = 16$. A uniform Cartesian mesh with a grid spacing of unity is employed to subdivide this domain. Initially, the region bounded by $y_L = 4L_0$ and $y_H = 12L_0$ is filled up with the liquid fluid, while the rest is occupied by the gas fluid. The periodic boundary condition is applied to all the sides. The relaxation time τ was fixed at 0.3. The CFL number was set as 0.5. The reduced temperature $T_r = T/T_c$ ranged from 0.55 to 0.95. The density field is initialized by

$$\rho(x,y) = \rho_g + \frac{\rho_l - \rho_g}{2} \left[\tanh\frac{2(y - y_L)}{W} - \tanh\frac{2(y - y_H)}{W} \right], \tag{47}$$

where W measures the interface thickness and ρ_l and ρ_g represent the liquid density and the gas density, respectively. Three reconstruction schemes were utilized to explore the influences of varying reconstruction errors on the performance of the DUGKS coupled with different free-energy models. Figure 1a illustrates the coexisting curves predicted by the DUGKS coupled with the primitive free-energy model. It can be observed that varying the reconstruction schemes offers different coexisting results. The central difference face-based reconstruction scheme (CD-FRS) provides satisfactory results in conditions of a high reduced temperature T_r. As T_r decreases, the results deviate apparently from the theoretical results generated by the Maxwell equal-area law [61]. The WENO-Z face-based reconstruction scheme (WENO-Z-FRS) and the upwind cell-based reconstruction scheme (CRS) produce inconsistent results in conditions of high T_r. As T_r decreases, both of them suffer from the stability problem. The fact that different reconstruction schemes generate divergent outcomes results from the force imbalance in the primitive free-energy model [30]. As the standard LB method involves no reconstruction process, the influences of the force imbalance on the numerical results remain limited. When it is coupled with numerical methods containing a reconstruction process, the effect of the force imbalance becomes amplified by the reconstruction errors. Figure 1b illustrates the results produced by the DUGKS coupled with the well-balanced free-energy model, in which the force imbalance was entirely eliminated. It can be identified that the coexisting densities predicted by different reconstruction schemes coincide exactly with the theoretical results. Moreover, the DUGKS implemented with different reconstruction schemes performs equally well in conditions of a low reduced temperature T_r, which demonstrates the fundamental accuracy and stability of this method. Figure 2 illustrates the comparative chemical potential profiles produced by the DUGKS coupled with different free-energy models at $T_r = 0.75$, $\tau = 0.3$, $C = 0.5$. Regardless of the reconstruction schemes utilized, the well-balanced free-energy-based DUGKS provides a nearly constant chemical potential profile, while the primitive free-energy-based DUGKS offers a varied chemical potential profile across the interfaces. Taking a closer look at the comparative profiles, we can identify that the chemical potential value produced by the DUGKS coupled with the primitive model varies along with the reconstruction schemes used, which should be attributed to the differences in the reconstruction errors. The chemical potential produced by the DUGKS coupled with the well-balanced model holds a nearly constant value of 0.006126, which demonstrates the excellent performance of the well-balanced DUGKS in predicting steady two-phase systems governed by free-energy theory.
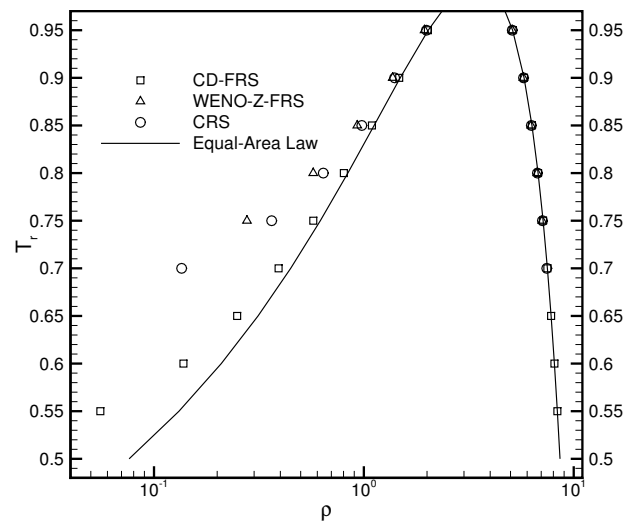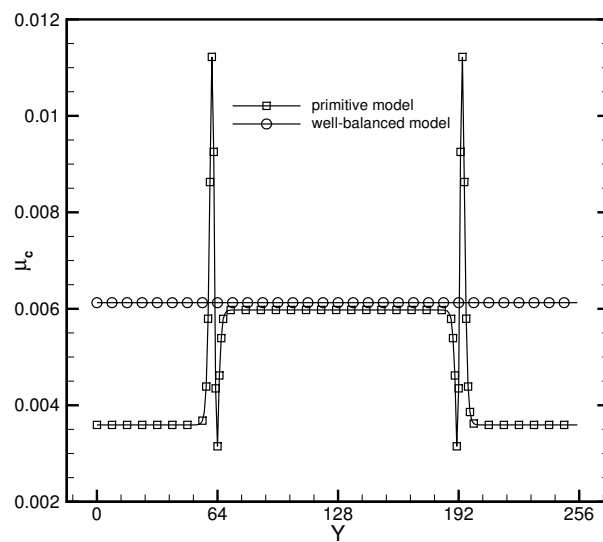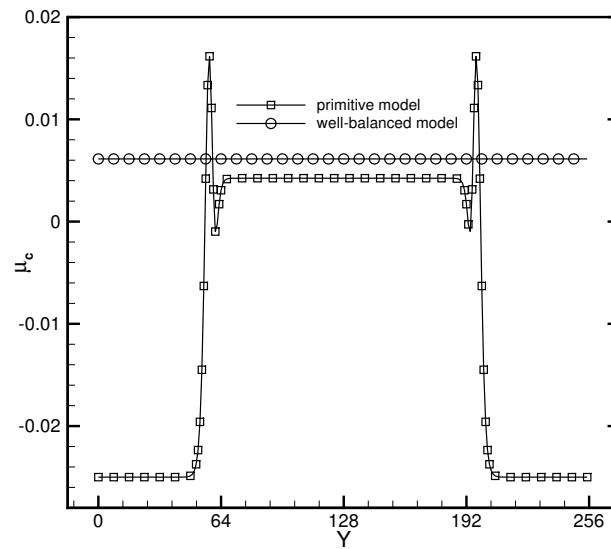
(**a**)
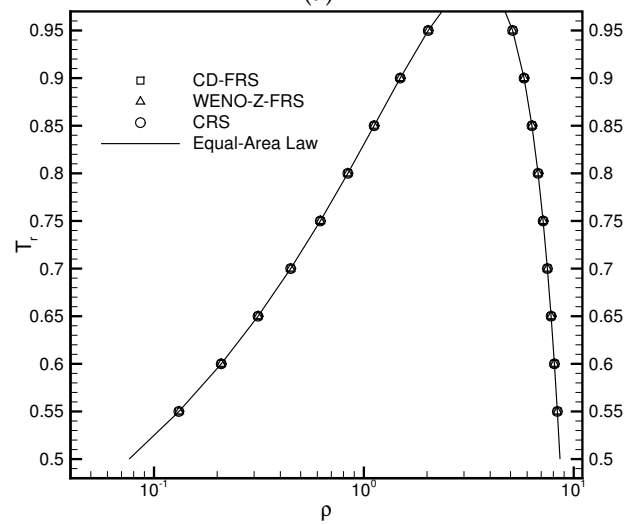
(**b**)

Figure 1. Coexisting curves produced by the DUGKS coupled with (**a**) primitive model and (**b**) well−balanced model, $\tau = 0.3$, $C = 0.5$.
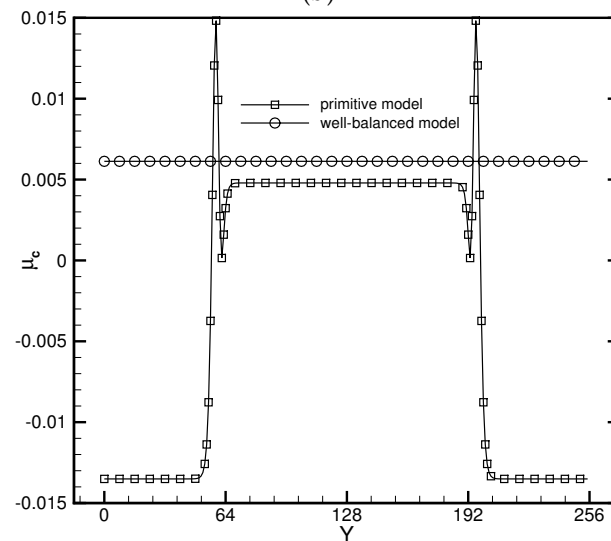

(**a**)

Figure 2. *Cont.*

(b)

(c)

Figure 2. Profiles of chemical potential μ_c produced by the DUGKS with (**a**) CD$-$FRS, (**b**) WENO$-$Z$-$FRS, and (**c**) CRS, $T_r = 0.75, \tau = 0.3, C = 0.5$.

3.2. Quiescent Droplet

The quiescent droplet test serves as one of the fundamental benchmarks for validating the basic capability of the newly proposed multiphase methods. A circular droplet is initially placed at the center of an $L_0 \times L_0$ square domain, with $L_0 = 256$. A uniform Cartesian mesh is used to discretize the physical domain, with the grid spacing Δx fixed at unity. The density field is initialized according to

$$\rho(x, y) = \frac{\rho_l + \rho_g}{2} - \frac{\rho_l - \rho_g}{2} \tanh \left[\frac{2 \left(\sqrt{|x - x_c|^2 + |y - y_c|^2} - R_d \right)}{W} \right], \tag{48}$$

where ρ_l and ρ_g correspond, respectively, to the coexisting liquid and gas densities, (x_c, y_c) indicates the center location of the square domain, R_d denotes the droplet radius, and W measures the interface thickness. The computing process terminates once the L_2-norm error of density evaluated by Equation (46) is below 10^{-10}. Figures 3–5 illustrate the density contours produced by the DUGKS coupled with different free-energy models and implemented by various reconstruction schemes at $T_r = 0.9, \tau = 0.6, C = 0.5$. The

interfaces produced with the primitive free-energy model suffer from the nonisotropic problem regardless of the reconstruction scheme utilized, which is caused by the force imbalance addressed previously. The second-order central-difference face-based reconstruction scheme (CD-FRS) evolves the initially circular interface into a roughly square interface, which should be attributed to the relatively large reconstruction errors. With a long time evolution, the fifth-order WENO-Z face-based reconstruction scheme (WENO-Z-FRS) shifts the quiescent droplet away from the center position. The interface profile deforms less than that produced by the CD-FRS, which might be attributed to the low level of reconstruction errors of WENO-Z. The interface profile generated by the third-order cell-based reconstruction scheme (CRS) is rather close to circular, which is due to the less nonisotropic reconstruction errors. A similar phenomenon can be observed in the results produced by the pseudopotential-based DUGKS. The interface profiles produced with the well-balanced free-energy model preserve a universal isotropic property across all reconstruction schemes, which demonstrates the elimination of the force imbalance. Figure 6 illustrates the contour of the velocity field produced by the DUGKS implemented with the CRS at $T_r = 0.9, \tau = 0.6, C = 0.5$. When the steady-state is reached, the velocity field produced by the primitive model exhibits a typical patten of large spurious currents, while the velocity field obtained with the well-balanced model provides spurious currents of machine accuracy. The excellent performance of the well-balanced DUGKS is thus verified by the comparative results.
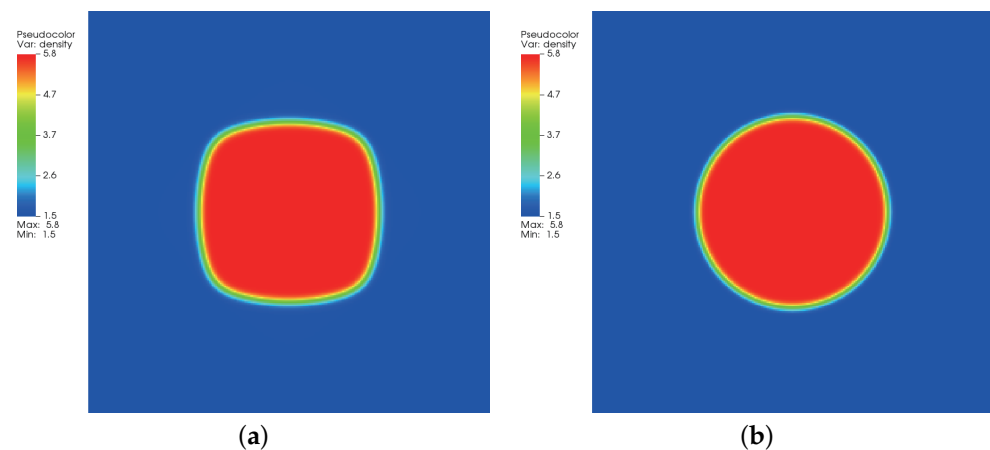

(a) **(b)**

Figure 3. Density contours produced by DUGKS implemented with CD-FRS coupled with (**a**) primitive model and (**b**) well-balanced model, $T_r = 0.9, \tau = 0.6, C = 0.5$.
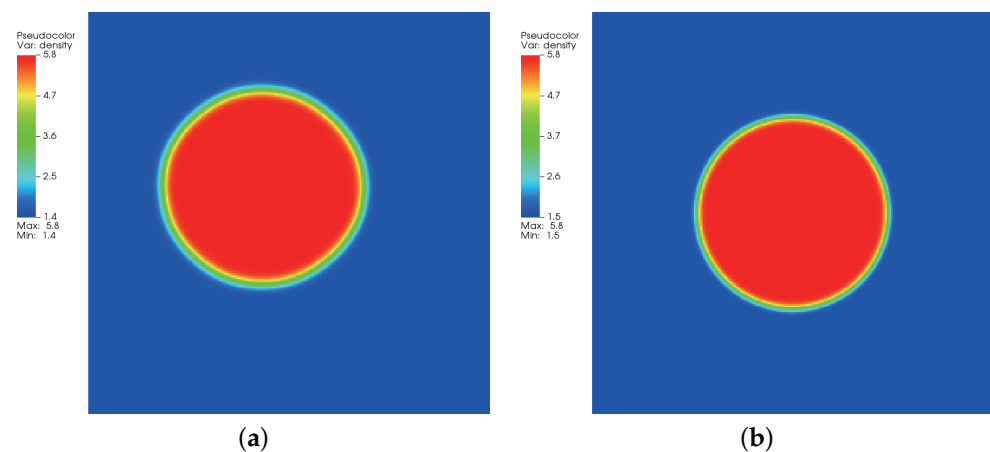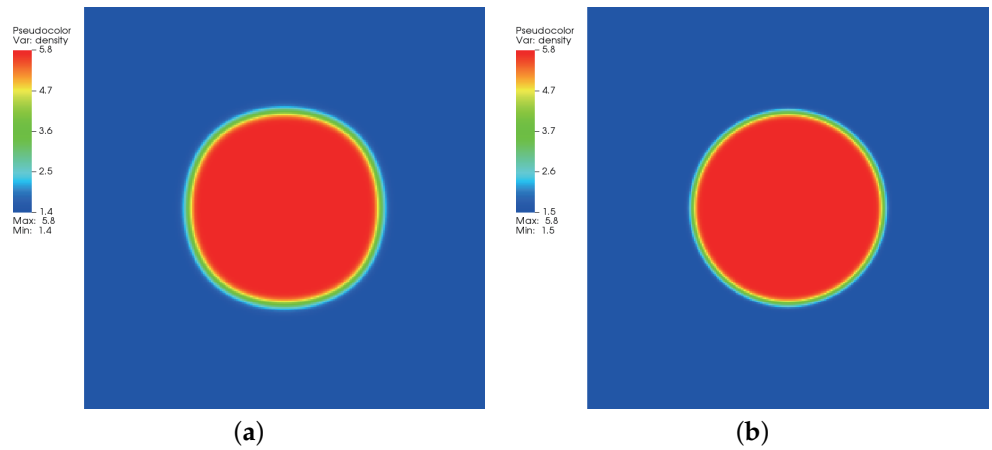

(a) **(b)**

Figure 4. Density contours produced by DUGKS implemented with WENO-Z-FRS coupled with (**a**) primitive model and (**b**) well-balanced model, $T_r = 0.9, \tau = 0.6, C = 0.5$.

Figure 5. Density contours produced by DUGKS implemented with CRS coupled with (**a**) primitive model and (**b**) well-balanced model, $T_r = 0.9$, $\tau = 0.6$, $C = 0.5$.
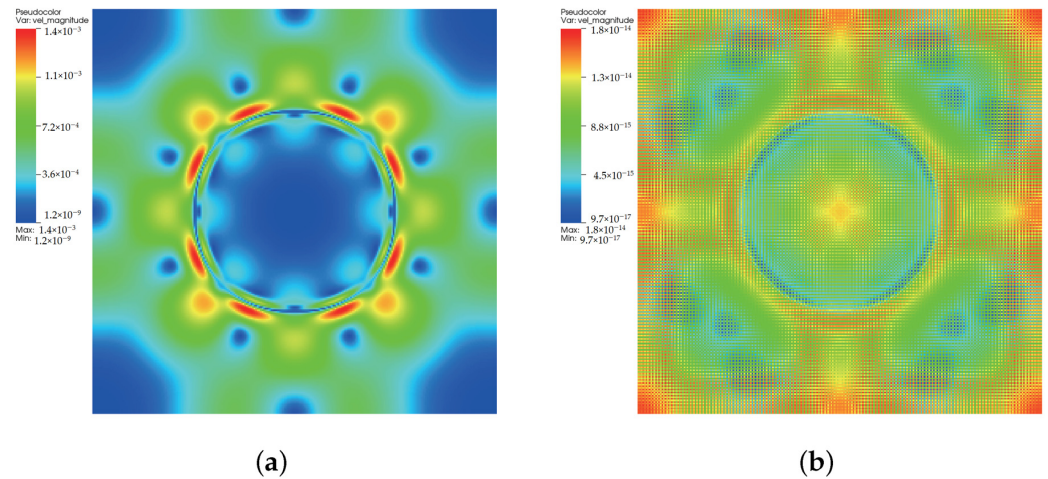

Figure 6. Velocity contours produced by DUGKS implemented with CRS coupled with (**a**) primitive model and (**b**) well-balanced model, $T_r = 0.9$, $\tau = 0.6$, $C = 0.5$.

To quantitatively assess its capability, Laplace's law is validated by the well-balanced DUGKS implemented with the CRS. Figure 7 illustrates the relations between the pressure jump ΔP and the reciprocal of radius R_d obtained at $\tau = 0.3$, $C = 0.8$. The linear relation can be clearly identified from the results, which conforms to Laplace's law: $\Delta P = \sigma / R_d$. The chemical potential varies along with the reduced temperature T_r, which results in the alteration of the surface tension coefficient σ. The CFL number was set as 0.8, at which the FRS fails to operate properly. The stability superiority of the CRS over that of the FRS in the condition of a large time step size makes it more appealing for multiphase flow simulations.

3.3. Spinodal Decomposition

Previous benchmark tests were limited to steady-state problems. Here, the spinodal decomposition test was adopted to assess the capability of DUGKS in dealing with transient problems. The computational domain is an $L_0 \times L_0$ square region subdivided by the uniform Cartesian mesh. The grid spacing $\Delta x = 1$, and the characteristic length $L_0 = 512$. The periodic boundary condition was applied to all the sides. The density field is initialized by

$$\rho(x, y) = (\rho_l + \rho_g)/3 + \text{random}(0, 1)/100, \tag{49}$$

where ρ_l and ρ_g represent the liquid density and the gas density and $\text{random}(0, 1)$ creates density fluctuations that induce the spinodal decomposition process. Figures 8–12 illustrate

the snapshots of the density distribution produced by the DUGKS coupled with the well-balanced free-energy model at $T_r = 0.9$, $\tau = 0.6$, $C = 0.5$. In the early stages, the tiny fluctuations generate local inhomogeneities, which initialize the phase separation. As the system evolves, the inhomogeneities drive the material of the heavy fluid into small droplets and interfaces separating different phases begin to emerge. With the continual evolution of the whole system, some of these droplets gradually coalesce into large ones. Eventually, a complete quiescent droplet is formed. It can be identified that the results produced by the central difference face-based reconstruction scheme (CD-FRS) are nearly identical to those generated by the third-order cell-based reconstruction scheme (CRS), which demonstrates the consistent behaviors of the well-balanced DUGKS. The WENO-Z face-based reconstruction scheme (WENO-Z-FRS) fails to provide a converged solution in such a condition. Moreover, the well-balanced DUGKS fails to predict the evolution process of the spinodal decomposition when the reduced temperature is below 0.8. To investigate the multiphase flow dynamics by the well-balanced DUGKS, further improvements are required.
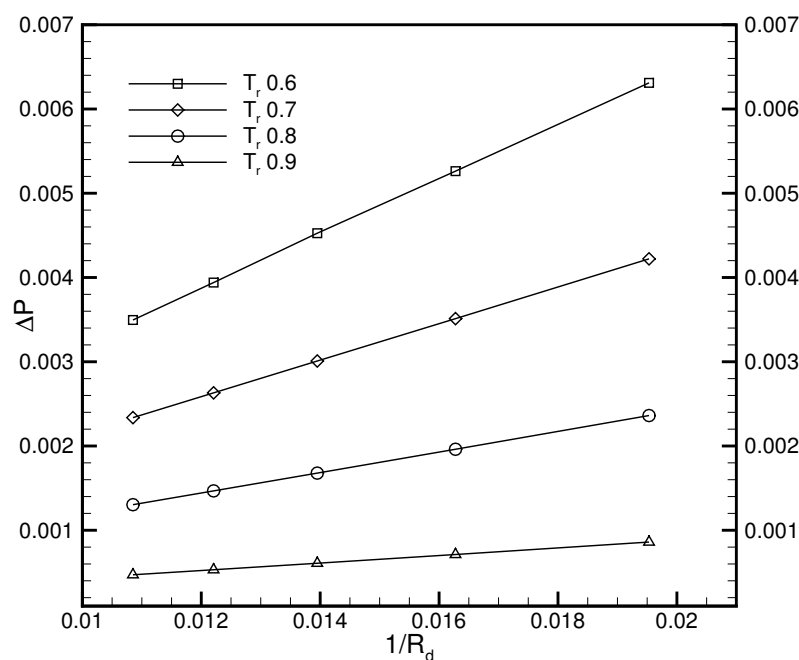

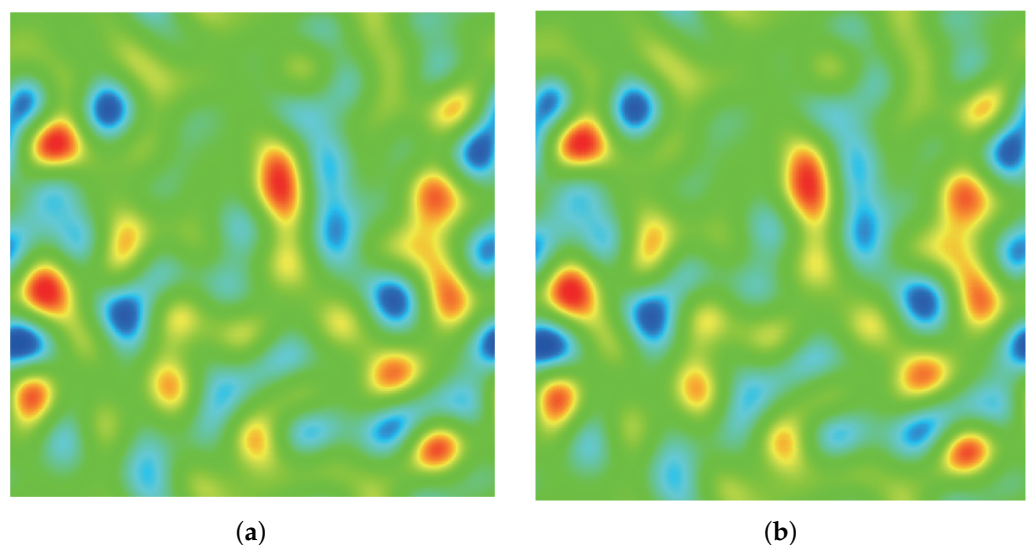**Figure 7.** Validation of Laplace's law, $\tau = 0.3$, $C = 0.8$.

Figure 8. Snapshots of the density distribution produced by the DUGKS implemented with (**a**) CD−FRS and (**b**) CRS, $T_r = 0.9$, $\tau = 0.6$, $C = 0.5$, $t = 2,500$.
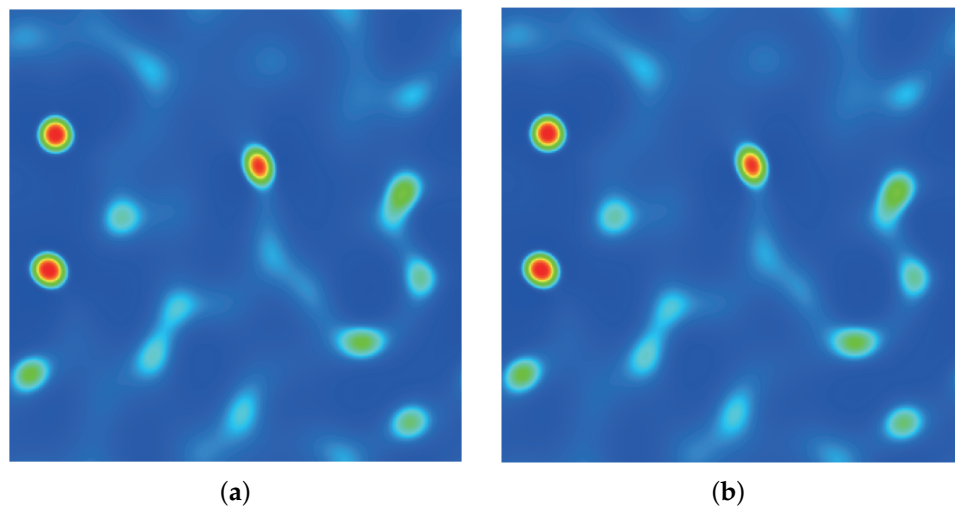
Figure 9. Snapshots of the density distribution produced by the DUGKS implemented with (**a**) CD−FRS and (**b**) CRS, $T_r = 0.9$, $\tau = 0.6$, $C = 0.5$, $t = 6,000$.
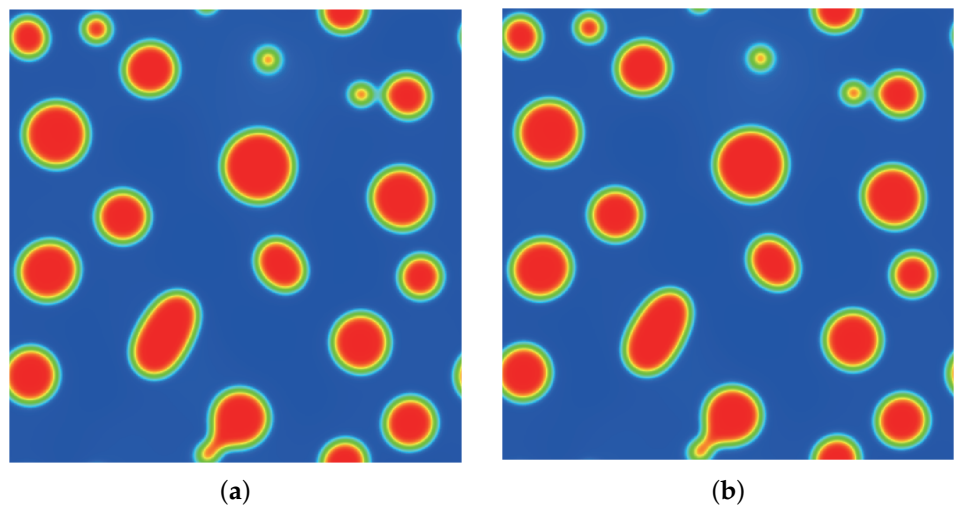

Figure 10. Snapshots of the density distribution produced by the DUGKS implemented with (**a**) CD−FRS and (**b**) CRS, $T_r = 0.9$, $\tau = 0.6$, $C = 0.5$, $t = 7,500$.
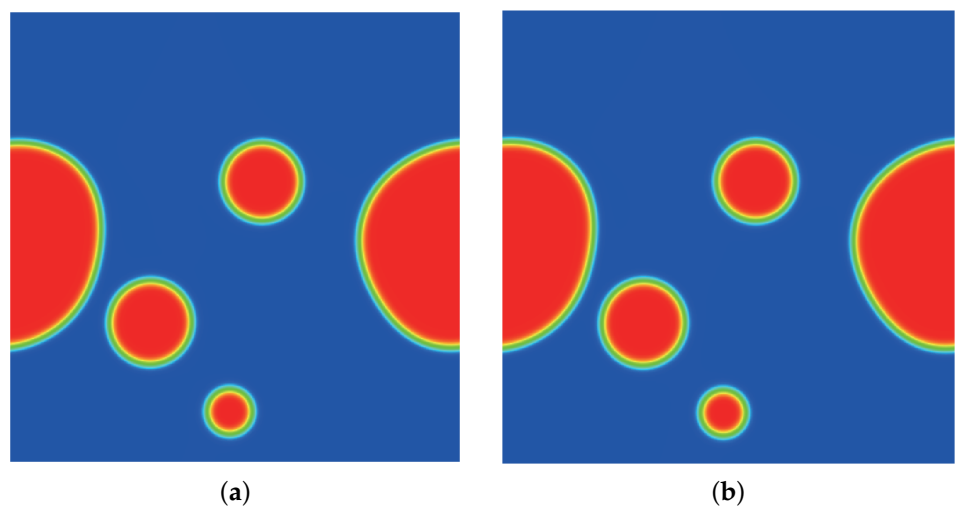

Figure 11. Snapshots of the density distribution produced by the DUGKS implemented with (**a**) CD−FRS and (**b**) CRS, $T_r = 0.9$, $\tau = 0.6$, $C = 0.5$, $t = 25,000$.
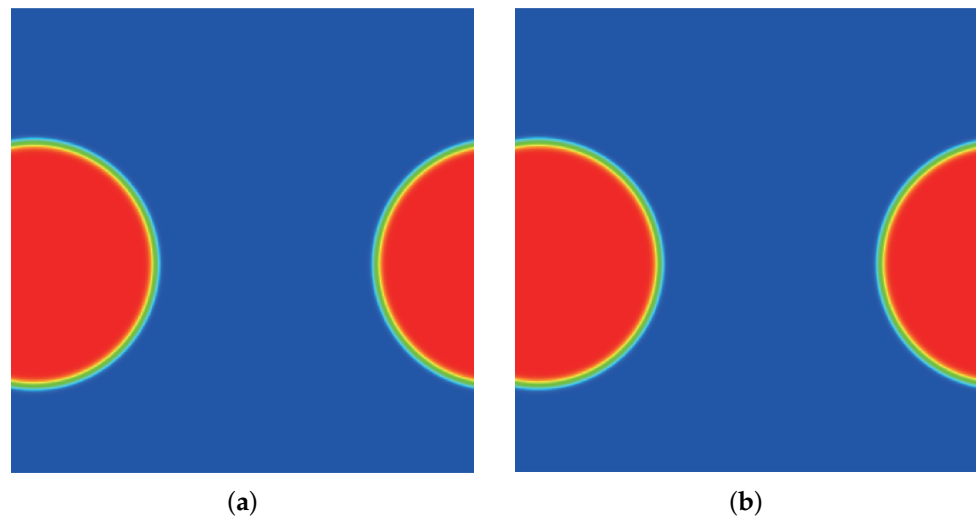
Figure 12. Snapshots of the density distribution produced by the DUGKS implemented with (**a**) CD−FRS and (**b**) CRS, $T_r = 0.9$, $\tau = 0.6$, $C = 0.5$, $t = 250{,}000$.

3.4. Droplet Coalescence

Simulations of the droplet coalescence phenomenon were used to further investigate the capacity of the well-balanced DUGKS for transient problems. The computational domain is a rectangle $2L_0 \times L_0$ domain with $L_0 = 256$. The domain was subdivided into finite grid cells by a uniform Cartesian mesh with a grid spacing of unity. To avoid wall boundary influence, a periodic boundary condition was used in all directions. Initially, two circular droplets were arranged in accordance with [51]

$$\rho(x, y) = \frac{\rho_l + \rho_g}{2} + \frac{\rho_l - \rho_g}{2}\left[1 - \tanh\left(\frac{2d_A}{W}\right) - \tanh\left(\frac{2d_B}{W}\right)\right], \qquad (50)$$

where ρ_l and ρ_g correspond separately to the liquid and gas densities, W measures the interface thickness, and d_A and d_B are defined as

$$d_A = \sqrt{(x - x_A)^2 + (y - y_A)^2} - R_0, \ d_B = \sqrt{(x - x_B)^2 + (y - y_B)^2} - R_0, \qquad (51)$$

in which R_0 denotes the droplet radius and $(x_A, y_A) = (L_0 - R_0 - W/2, L_0/2)$ and $(x_B, y_B) = (L_0 + R_0 + W/2, L_0/2)$ represent the central position of droplets A and B, respectively. Other parameters were set as $\kappa = 0.02$, $R_0 = 0.2L_0$, $W = 5$, and $\tau = 0.3$. The initial profile of two droplets is illustrated in Figure 13. The coalescence process starts when the droplets come in contact with each other. As the process continues, a liquid bridge of radius r_b that connects the two droplets is formed [51]. Previous research [62] identified the linear relation between the scaled radius r^* and the dimensionless time t^*, with

$$r^* = r_b/R_0, \ t^* = t/\sqrt{\rho_l R_0^3 \sigma}, \qquad (52)$$

where σ is the surface tension coefficient. According to the validation of Laplace's law illustrated in Figure 7, the surface tension coefficient is 0.1203 for $T_r = 0.8$ and 0.0435 for $T_r = 0.9$. Figure 14 presents the radius variation of the liquid bridge with regard to the dimensionless time t^*. The linear coefficient for the fitting result provided by the DUGKS using the primitive model is 1.4, while the linear coefficient for the fitting result produced with the well-balanced model is 1.03, which is in good agreement with the result predicted by Zeng et al. [51]. The evolution of the L_2-norm of the velocity field produced by the DUGKS using the well-balanced model at $T_r = 0.8$ and $T_r = 0.9$ is shown in Figure 15. It can be identified that the L_2-norm of the velocity field reaches a magnitude of 10^{-14}, which is consistent with the results predicted at the steady-state. Figure 16 illustrates the density and velocity contours produced by the well-balanced DUGKS at $t = 6 \times 10^6$, $T_r = 0.8$,

$\tau = 0.3$, $C = 0.8$. It can be observed that the interface maintains excellent isotropy and the velocity field holds a maximum magnitude of 10^{-16}, which demonstrates the excellent ability of the well-balanced DUGKS. However, it is important to note that when the lowered temperature T_r is less than 0.7, the DUGKS is unable to predict the coalescence process. More efforts are required to increase the stability of the well-balanced DUGKS.
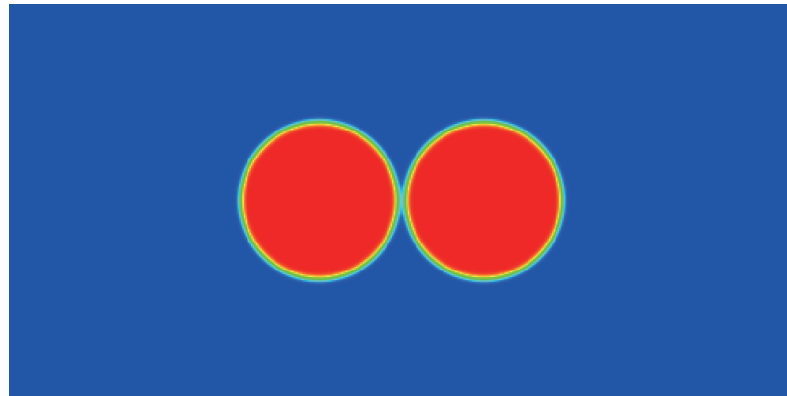

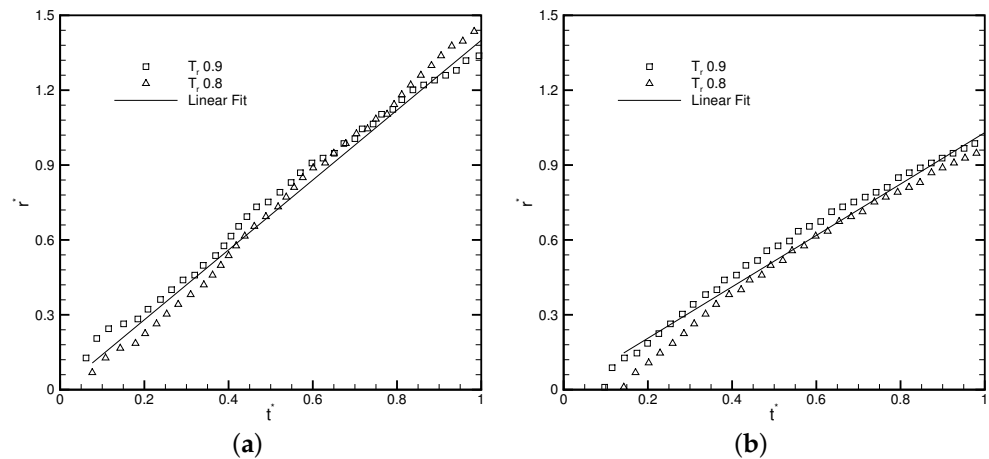**Figure 13.** Initial distribution of the density field.

Figure 14. Radius variation of the liquid bridge with regard to the dimensionless time produced by DUGKS coupled with (**a**) primitive model and (**b**) well−balanced model, $\tau = 0.3$, $C = 0.8$.
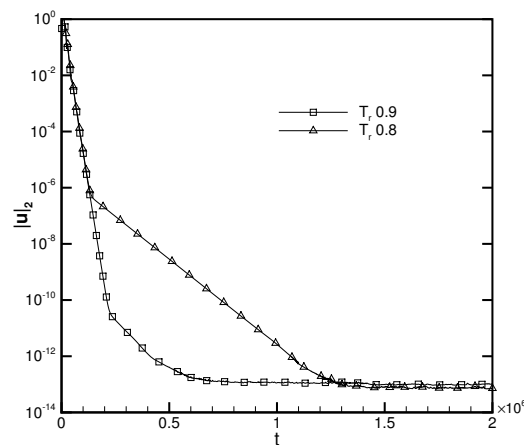

Figure 15. L_2−norm of the velocity field produced by the well-balanced DUGKS with the evolution of time, $\tau = 0.3$, $C = 0.8$.
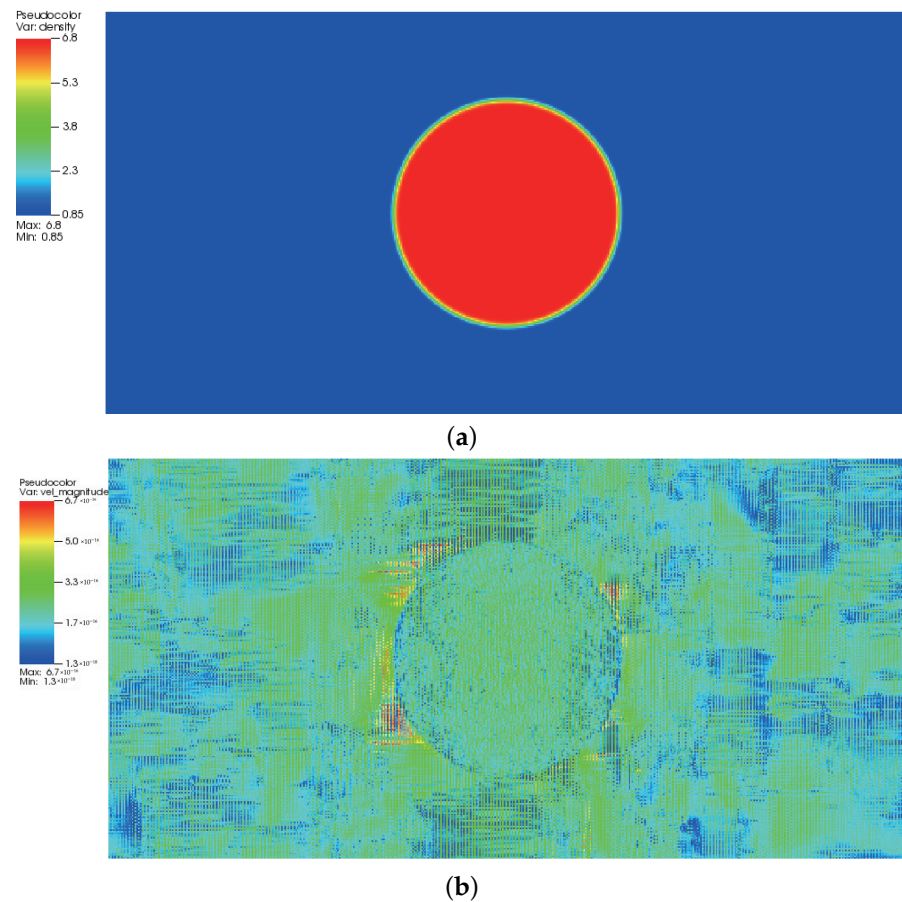
(**a**)

(**b**)

Figure 16. Contours of (**a**) density field and (**b**) velocity field produced by the well-balanced DUGKS at $t = 6 \times 10^6$, $T_r = 0.8$, $\tau = 0.3$, $C = 0.8$.

4. Conclusions

A free-energy-based discrete unified gas-kinetic scheme (DUGKS) was developed by coupling the well-balanced free-energy model with the DUGKS to investigate the van der Waals fluid. The performance of this well-balanced scheme was compared against the counterpart of the DUGKS coupled with the primitive free-energy model. Comparative results produced with different reconstruction schemes demonstrated the force imbalance in the primitive free-energy model, which prevents its direct application to the DUGKS. By coupling the well-balanced free-energy model with the DUGKS, the amplified effects of the force imbalance are entirely eliminated and the influences of nonisotropic reconstruction errors on the fluid interfaces are totally removed. Numerical tests of a flat interface, quiescent droplet, spinodal decomposition, and droplet coalescence were adopted to assess the performance of the DUGKS coupled with the well-balanced free-energy model. Coexisting density curves and Laplace's law were utilized to evaluate its capability quantitatively. It was proven that the well-balanced DUGKS could always produce consistent results despite the reconstruction schemes utilized in steady cases. When dealing with transient problems, the reconstruction scheme employing WENO-Z to evaluate face unknowns tends to be more unstable. When the reduced temperature is below 0.7, the DUGKS coupled with the well-balanced free-energy model suffers from stability problems. Further improvements are required to apply this scheme to predict transient multiphase fluid flows.

Author Contributions: Z.Y.: methodology, software, validation, formal analysis, data curation, writing—original draft preparation. S.L.: funding acquisition, methodology, writing—review and editing. C.Z. (Congshan Zhuo): supervision, funding acquisition, resources, investigation, writing–review and editing. C.Z. (Chengwen Zhong): project administration, funding acquisition, conceptual-

Appendix A. Nondimensionalization of the Boltzmann-BGK Equation

The nondimensionalization process of the Boltzmann-BGK equation is analyzed in this part. The dimensional Boltzmann-BGK equation with a source term reads

$$\frac{\partial f}{\partial t} + \boldsymbol{\xi} \cdot \nabla_x f = -\frac{1}{\tau}\left(f - f^{\mathrm{E}}\right) + f^{\mathrm{S}}, \tag{A1}$$

where f represents the distribution function, t is the time, x is the position, $\boldsymbol{\xi}$ is the particle velocity, τ is the relaxation time, f^{E} indicates the equilibrium distribution function, and f^{S} accounts for the source distribution function. Introducing the characteristic length l_c, the characteristic velocity u_c, the characteristic density ρ_c, and multiplying Equation (A1) by $l_c/(\rho_c u_c)$ on both sides, we have

$$\frac{\partial f^*}{\partial t^*} + \boldsymbol{\xi}^* \cdot \nabla_{x^*} f^* = -\frac{l_c}{u_c \tau}\left(f^* - f^{\mathrm{E},*}\right) + f^{\mathrm{S},*}, \tag{A2}$$

where

$$t^* = \frac{t u_c}{l_c}, \boldsymbol{\xi}^* = \frac{\boldsymbol{\xi}}{u_c}, \boldsymbol{x}^* = \frac{\boldsymbol{x}}{l_c}, f^* = \frac{f}{\rho_c}, f^{\mathrm{E},*} = \frac{f^{\mathrm{E}}}{\rho_c}, f^{\mathrm{S},*} = \frac{f^{\mathrm{S}} l_c}{\rho_c u_c}. \tag{A3}$$

As the relaxation time τ is evaluated by $\tau = \mu/\rho_c c_s^2$, where μ is the dynamic viscosity, the multiplier $l_c/(u_c \tau)$ becomes

$$\frac{l_c}{u_c \tau} = \frac{l_c \rho_c c_s^2}{u_c \mu} = \frac{\mathrm{Re}}{\mathrm{Ma}}, \tag{A4}$$

where

$$\mathrm{Ma} = \frac{u_c}{c_s}, \mathrm{Re} = \frac{\rho_c l_c c_s}{\mu}. \tag{A5}$$

Equation (A2) turns into

$$\frac{\partial f^*}{\partial t^*} + \boldsymbol{\xi}^* \cdot \nabla_{x^*} f^* = -\frac{\mathrm{Re}}{\mathrm{Ma}}\left(f^* - f^{\mathrm{E},*}\right) + f^{\mathrm{S},*}, \tag{A6}$$

which is the dimensionless Boltzmann-BGK equation. In multiphase simulation involving droplet dynamics, the Reynolds number is generally defined as

$$\mathrm{Re}_d = \frac{\rho_c u_c l_c}{\mu}. \tag{A7}$$

With this definition, the dimensionless Boltzmann-BGK equation becomes

$$\frac{\partial f^*}{\partial t^*} + \boldsymbol{\xi}^* \cdot \nabla_{x^*} f^* = -\frac{\mathrm{Re}_d}{\mathrm{Ma}^2}\left(f^* - f^{\mathrm{E},*}\right) + f^{\mathrm{S},*}. \tag{A8}$$

References

1. Hirt, C.; Nichols, B. Volume of fluid (VOF) method for the dynamics of free boundaries. *J. Comput. Phys.* **1981**, *39*, 201–225.
2. Unverdi, S.O.; Tryggvason, G. A front-tracking method for viscous, incompressible, multi-fluid flows. *J. Comput. Phys.* **1992**, *100*, 25–37.
3. Anderson, D.M.; McFadden, G.B.; Wheeler, A.A. Diffuse-interface methods in fluid mechanics. *Annu. Rev. Fluid Mech.* **1998**, *30*, 139–165.
4. Sethian, J.A.; Smereka, P. Level set methods for fluid interfaces. *Annu. Rev. Fluid Mech.* **2003**, *35*, 341–372.
5. Guo, Z.; Zheng, C.; Shi, B. Force imbalance in lattice Boltzmann equation for two-phase flows. *Phys. Rev. E* **2011**, *83*, 036707.
6. Fox, R.O. Large-eddy-simulation tools for multiphase flows. *Annu. Rev. Fluid Mech.* **2012**, *44*, 47–76.
7. Aidun, C.K.; Clausen, J.R. Lattice-Boltzmann method for complex flows. *Annu. Rev. Fluid Mech.* **2010**, *42*, 439–472.
8. Gan, Y.; Xu, A.; Zhang, G.; Succi, S. Discrete Boltzmann modeling of multiphase flows: hydrodynamic and thermodynamic non-equilibrium effects. *Soft Matter* **2015**, *11*, 5336–5345.
9. Wang, Y.; Shu, C.; Shao, J.; Wu, J.; Niu, X. A mass-conserved diffuse interface method and its application for incompressible multiphase flows with large density ratio. *J. Comput. Phys.* **2015**, *290*, 336–351.
10. Gunstensen, A.K.; Rothman, D.H.; Zaleski, S.; Zanetti, G. Lattice Boltzmann model of immiscible fluids. *Phys. Rev. A* **1991**, *43*, 4320–4327.
11. He, X.; Chen, S.; Zhang, R. A lattice Boltzmann scheme for incompressible multiphase flow and its application in simulation of Rayleigh-Taylor instability. *J. Comput. Phys.* **1999**, *152*, 642–663.
12. Geier, M.; Fakhari, A.; Lee, T. Conservative phase-field lattice Boltzmann model for interface tracking equation. *Phys. Rev. E* **2015**, *91*, 063309.
13. Shan, X.; Chen, H. Lattice Boltzmann model for simulating flows with multiple phases and components. *Phys. Rev. E* **1993**, *47*, 1815–1819.
14. Swift, M.R.; Osborn, W.R.; Yeomans, J.M. Lattice Boltzmann simulation of nonideal fluids. *Phys. Rev. Lett.* **1995**, *75*, 830–833.
15. Yang, K.; Guo, Z. Lattice Boltzmann method for binary fluids based on mass-conserving quasi-incompressible phase-field theory. *Phys. Rev. E* **2016**, *93*, 043303.
16. Briant, A.J.; Wagner, A.J.; Yeomans, J.M. Lattice Boltzmann simulations of contact line motion. I. Liquid-gas systems. *Phys. Rev. E* **2004**, *69*, 031602.
17. Briant, A.J.; Yeomans, J.M. Lattice Boltzmann simulations of contact line motion. II. Binary fluids. *Phys. Rev. E* **2004**, *69*, 031603.
18. Li, Q.; Wagner, A.J. Symmetric free-energy-based multicomponent lattice Boltzmann method. *Phys. Rev. E* **2007**, *76*, 036701.
19. Zhang, J.; Kwok, D.Y. A mean-field free energy lattice Boltzmann model for multicomponent fluids. *Eur. Phys. J. Spec. Top.* **2009**, *171*, 45–53.
20. Wiklund, H.; Lindström, S.; Uesaka, T. Boundary condition considerations in lattice Boltzmann formulations of wetting binary fluids. *Comput. Phys. Commun.* **2011**, *182*, 2192–2200.
21. Wen, B.; Huang, B.; Qin, Z.; Wang, C.; Zhang, C. Contact angle measurement in lattice Boltzmann method. *Comput. Math. Appl.* **2018**, *76*, 1686–1698.
22. Yan, Y.; Zu, Y. A lattice Boltzmann method for incompressible two-phase flows on partial wetting surface with large density ratio. *J. Comput. Phys.* **2007**, *227*, 763–775.
23. Wen, B.; Zhao, L.; Qiu, W.; Ye, Y.; Shan, X. Chemical-potential multiphase lattice Boltzmann method with superlarge density ratios. *Phys. Rev. E* **2020**, *102*, 013303.
24. Swift, M.R.; Orlandini, E.; Osborn, W.R.; Yeomans, J.M. Lattice Boltzmann simulations of liquid-gas and binary fluid systems. *Phys. Rev. E* **1996**, *54*, 5041–5052.
25. Inamuro, T.; Konishi, N.; Ogino, F. A Galilean invariant model of the lattice Boltzmann method for multiphase fluid flows using free-energy approach. *Comput. Phys. Commun.* **2000**, *129*, 32–45.
26. Kalarakis, A.N.; Burganos, V.N.; Payatakes, A.C. Galilean-invariant lattice-Boltzmann simulation of liquid-vapor interface dynamics. *Phys. Rev. E* **2002**, *65*, 056702.
27. Wagner, A.; Li, Q. Investigation of Galilean invariance of multi-phase lattice Boltzmann methods. *Phys. A Stat. Mech. Appl.* **2006**, *362*, 105–110.
28. Lee, T.; Fischer, P.F. Eliminating parasitic currents in the lattice Boltzmann equation method for nonideal gases. *Phys. Rev. E* **2006**, *74*, 046709.
29. Lou, Q.; Guo, Z. Interface-capturing lattice Boltzmann equation model for two-phase flows. *Phys. Rev. E* **2015**, *91*, 013302.
30. Guo, Z. Well-balanced lattice Boltzmann model for two-phase systems. *Phys. Fluids* **2021**, *33*, 031709.
31. Guo, Z.; Xu, K.; Wang, R. Discrete unified gas kinetic scheme for all Knudsen number flows: Low-speed isothermal case. *Phys. Rev. E* **2013**, *88*, 033305.
32. Guo, Z.; Wang, R.; Xu, K. Discrete unified gas kinetic scheme for all Knudsen number flows. II. Thermal compressible case. *Phys. Rev. E* **2015**, *91*, 033313.
33. Zhu, L.; Guo, Z. Numerical study of nonequilibrium gas flow in a microchannel with a ratchet surface. *Phys. Rev. E* **2017**, *95*, 023113.

34. Liu, H.; Cao, Y.; Chen, Q.; Kong, M.; Zheng, L. A conserved discrete unified gas kinetic scheme for microchannel gas flows in all flow regimes. *Comput. Fluids* **2018**, *167*, 313–323.
35. Zhang, Y.; Zhu, L.; Wang, R.; Guo, Z. Discrete unified gas kinetic scheme for all Knudsen number flows. III. Binary gas mixtures of Maxwell molecules. *Phys. Rev. E* **2018**, *97*, 053306.
36. Zhang, Y.; Zhu, L.; Wang, P.; Guo, Z. Discrete unified gas kinetic scheme for flows of binary gas mixture based on the McCormack model. *Phys. Fluids* **2019**, *31*, 017101.
37. Wang, P.; Wang, L.P.; Guo, Z. Comparison of the lattice Boltzmann equation and discrete unified gas-kinetic scheme methods for direct numerical simulation of decaying turbulent flows. *Phys. Rev. E* **2016**, *94*, 043304.
38. Bo, Y.; Wang, P.; Guo, Z.; Wang, L.P. DUGKS simulations of three-dimensional Taylor–Green vortex flow and turbulent channel flow. *Comput. Fluids* **2017**, *155*, 9–21.
39. Zhang, R.; Zhong, C.; Liu, S.; Zhuo, C. Large-eddy simulation of wall-bounded turbulent flow with high-order discrete unified gas-kinetic scheme. *Adv. Aerodyn.* **2020**, *2*, 26.
40. Chen, J.; Liu, S.; Wang, Y.; Zhong, C. Conserved discrete unified gas-kinetic scheme with unstructured discrete velocity space. *Phys. Rev. E* **2019**, *100*, 043305.
41. Zhong, M.; Zou, S.; Pan, D.; Zhuo, C.; Zhong, C. A simplified discrete unified gas–kinetic scheme for compressible flow. *Phys. Fluids* **2021**, *33*, 036103.
42. Wen, X.; Wang, L.P.; Guo, Z.; Shen, J. An improved discrete unified gas kinetic scheme for simulating compressible natural convection flows. *J. Comput. Phys. X* **2021**, *11*, 100088.
43. Guo, Z.; Xu, K. Discrete unified gas kinetic scheme for multiscale heat transfer based on the phonon Boltzmann transport equation. *Int. J. Heat Mass Transf.* **2016**, *102*, 944–958.
44. Luo, X.P.; Wang, C.H.; Zhang, Y.; Yi, H.L.; Tan, H.P. Multiscale solutions of radiative heat transfer by the discrete unified gas kinetic scheme. *Phys. Rev. E* **2018**, *97*, 063302.
45. Guo, Z.; Xu, K. Progress of discrete unified gas-kinetic scheme for multiscale flows. *Adv. Aerodyn.* **2021**, *3*, 6.
46. Wang, P.; Zhu, L.; Guo, Z.; Xu, K. A comparative study of LBE and DUGKS methods for nearly incompressible flows. *Commun. Comput. Phys.* **2015**, *17*, 657–681.
47. Zhang, C.; Yang, K.; Guo, Z. A discrete unified gas-kinetic scheme for immiscible two-phase flows. *Int. J. Heat Mass Transf.* **2018**, *126*, 1326–1336.
48. Yang, Z.; Zhong, C.; Zhuo, C. Phase-field method based on discrete unified gas-kinetic scheme for large-density-ratio two-phase flows. *Phys. Rev. E* **2019**, *99*, 043302.
49. Yang, Z.; Liu, S.; Zhuo, C.; Zhong, C. Conservative multilevel discrete unified gas kinetic scheme for modeling multiphase flows with large density ratios. *Phys. Fluids* **2022**, *34*, 043316.
50. Yang, Z.; Liu, S.; Zhuo, C.; Zhong, C. Pseudopotential-based discrete unified gas kinetic scheme for modeling multiphase fluid flows. *Res. Sq.* **2022**, https://doi.org/10.21203/rs.3.rs-1808723/v1.
51. Zeng, W.; Zhang, C.; Guo, Z. Well-balanced discrete unified gas-kinetic scheme for two-phase systems. *Phys. Fluids* **2022**, *34*, 052111.
52. Jacqmin, D. Calculation of two-phase Navier-Stokes flows using phase-field modeling. *J. Comput. Phys.* **1999**, *155*, 96–127.
53. Goldstein, H.; Poole, C.; Safko, J. *Classical Mechanics*, 3rd ed.; Pearson: London, UK, 2001.
54. Sbragaglia, M.; Chen, H.; Shan, X.; Succi, S. Continuum free-energy formulation for a class of lattice Boltzmann multiphase models. *Europhys. Lett.* **2009**, *86*, 24005.
55. Wen, B.; Zhou, X.; He, B.; Zhang, C.; Fang, H. Chemical-potential-based lattice Boltzmann method for nonideal fluids. *Phys. Rev. E* **2017**, *95*, 063305.
56. Li, Q.; Yu, Y.; Huang, R.Z. Achieving thermodynamic consistency in a class of free-energy multiphase lattice Boltzmann models. *Phys. Rev. E* **2021**, *103*, 013304.
57. Yang, Z.; Zhong, C.; Zhuo, C.; Liu, S. Spatio-temporal error coupling and competition in meso-flux construction of discrete unified gas-kinetic scheme. *Comput. Fluids* **2022**, *244*, 105537.
58. Borges, R.; Carmona, M.; Costa, B.; Don, W.S. An improved weighted essentially non-oscillatory scheme for hyperbolic conservation laws. *J. Comput. Phys.* **2008**, *227*, 3191–3211.
59. Tao, S.; Zhang, H.; Guo, Z.; Wang, L.P. A combined immersed boundary and discrete unified gas kinetic scheme for particle–fluid flows. *J. Comput. Phys.* **2018**, *375*, 498–518.
60. Kumar, A. Isotropic finite-differences. *J. Comput. Phys.* **2004**, *201*, 109–118.
61. Chen, L.; Kang, Q.; Mu, Y.; He, Y.L.; Tao, W.Q. A critical review of the pseudopotential multiphase lattice Boltzmann model: Methods and applications. *Int. J. Heat Mass Transf.* **2014**, *76*, 210–236.
62. Wu, M.; Cubaud, T.; Ho, C.M. Scaling law in liquid drop coalescence driven by surface tension. *Phys. Fluids* **2004**, *16*, L51–L54.